J. Fluid Mech. (2003), *vol.* 482, *pp.* 271–290.
DOI: 10.1017/S0022112003004117 Printed in the United Kingdom

The added mass of an expanding bubble†

By C. D. OHL, A. TIJINK AND A. PROSPERETTI‡

Department of Applied Physics, Twente Institute of Mechanics and Burgerscentrum, University of Twente, AE 7500 Enschede, The Netherlands

(Received 7 December 2001 and in revised form 1 November 2002)

The added mass interaction of a body of variable volume translating in a fluid depends not only on the relative acceleration, but also on the rate of change of the volume. In the present study this prediction is put to an experimental test by observing the motion of a bubble rising in a pressurized tube. When the pressure is brought back to ambient by a fast-opening valve, the bubble expands and, from an analysis of its acceleration, it is possible to deduce the effect of the volume change on the added mass interaction. The results support the validity of the conventional theory for this effect. Some other observations on the transition from a straight to a spiral or zig-zag trajectory – a regime which may well be called 'Leonardo's paradox' – are reported.

1. Introduction

According to classical fluid dynamics, the Kelvin impulse $\boldsymbol{I}$ of a sphere in rectilinear motion in an infinite fluid is proportional to one-half the displaced fluid mass and the relative velocity $\boldsymbol{U}_r$ with respect to the fluid (see e.g. Lamb 1932, art. 92; Benjamin & Ellis 1966; Landau & Lifshitz 1987, section 11):

$$\boldsymbol{I} = \tfrac{1}{2}\rho\left(\tfrac{4}{3}\pi R^3\right)\boldsymbol{U}_r; \tag{1}$$

here ρ is the fluid density and R the radius of the sphere. Any attempt to change $\boldsymbol{U}_r$ must overcome the inertia of the body, but also the reaction $-\mathrm{d}\boldsymbol{I}/\mathrm{d}t$ of the surrounding fluid; conversely, any change in $\boldsymbol{I}$ must affect the dynamics of the body.

In typical applications of this result, R is fixed and $\boldsymbol{I}$ changes because $\boldsymbol{U}_r$ does; however, according to (1), $\boldsymbol{I}$ can also change due to changes in R. While this fact is widely appreciated in the theoretical literature (see e.g. Lhuillier 1982; Wallis 1989; Magnaudet & Legendre 1998; Sherwood 1999; Magnaudet & Eames 2000), it does not seem to have ever been subjected to an experimental test. The purpose of this paper is to describe the results of an experiment in which the dependence of the Kelvin impulse on R is tested directly for a small, millimetre-sized bubble. The bubble ascends in a pressurized vertical tube: when the pressure in the tube is brought back to atmospheric, the bubble expands, its Kelvin impulse changes, and the rise velocity is temporarily affected.

Here we analyse the data in terms of a simple model; a companion paper (Yang, Prosperetti & Takagi 2003) presents the results of a direct numerical simulation.

† With an Appendix by A. Prosperetti, C. D. Ohl, A. Tijink, G. Mougin & J. Magnaudet.

‡ Permanent address: Department of Mechanical Engineering, The Johns Hopkins University, Baltimore, MD 21218, USA.

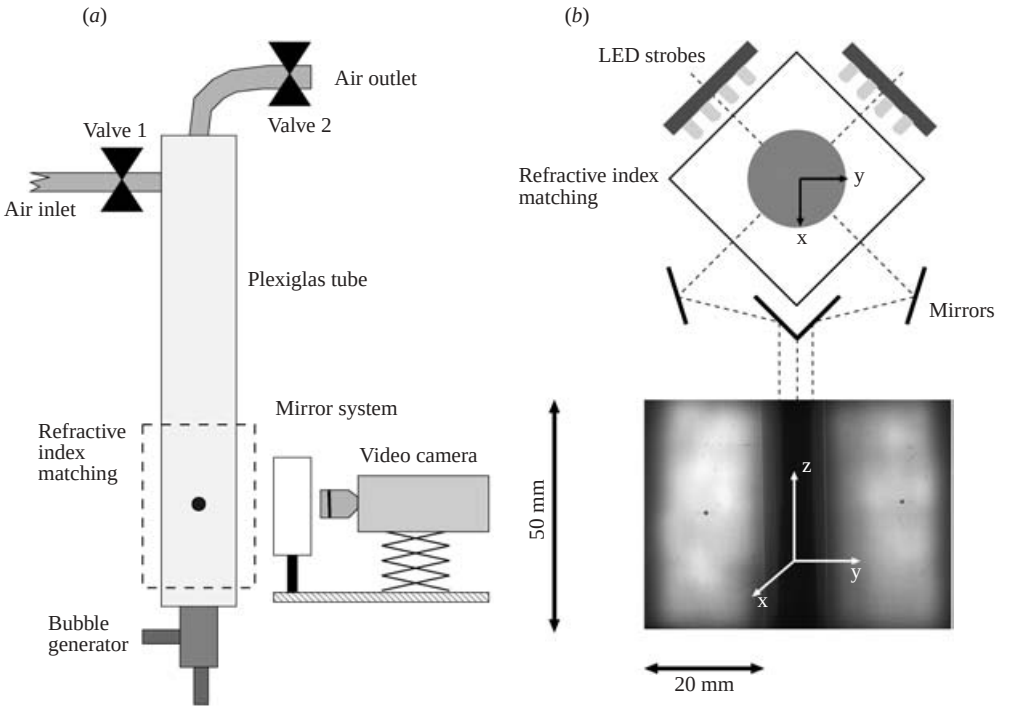

FIGURE 1. Sketch of (*a*) the experimental set-up and (*b*) the optical system. Valve 1 is used to pressurize the Plexiglas tube and the fast-opening valve 2 permits a fast return to atmospheric pressure. The four mirrors give a simultaneous recording of the bubble image in two orthogonal planes. An example of the two images with the coordinate system is shown in the lower part of (*b*).

2. Experimental set-up

The experimental set-up consists of a bubble generator, a vertical Plexiglas tube of 2 m height and 50 mm internal diameter, and an imaging section near the bottom of the tube (figure 1*a*). The tube is filled with deionized and filtered water from a Micropore purification system (RO 60) to about 0.2 m from the top, taking care to avoid the entrapment of residual gas pockets. The gas space is pressurized by high-pressure air regulated by a Ni-C Span manometer (Budenberg Manchester) and an electrically controlled valve. Depressurization is achieved by means of a second electrically controlled solenoid valve. Both valves are controlled by solid-state relays triggered with a signal from a PC. The pressure in the air space is measured with a pressure sensor (PX203, Omega Inc.). The readings of this sensor were cross-checked with additional measurements in the liquid with a hydrophone (8103, Brül & Kjaer) connected to a charge amplifier: no appreciable difference between the two sets of measurements was found and, accordingly, only readings from the upper sensor are reported here.

Figure 2 depicts a typical pressure recording during the depressurization phase, for an over-pressure of about 3 bars. Except for some minor oscillations (due to elastic waves propagating along the tube – see Appendix A – and system vibrations), the pressure decrease is smooth and is completed in about 70 ms.

Single bubbles are injected at the bottom of the tube with a specially designed bubble generator described in Ohl (2001): an air bubble is injected at a T-junction

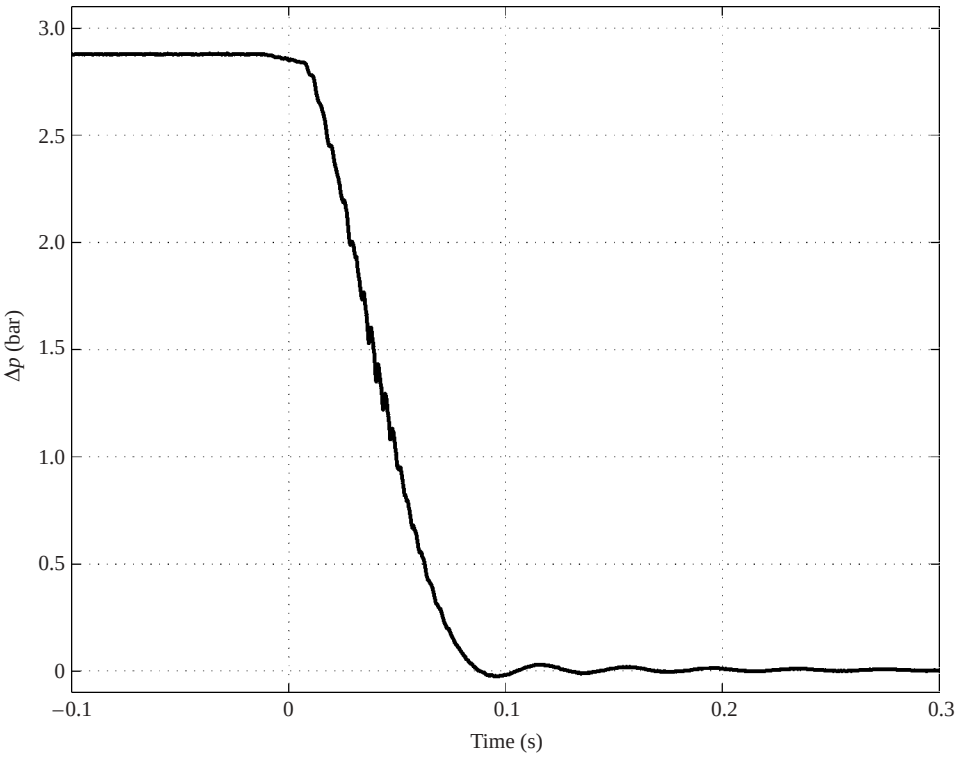

FIGURE 2. Static over-pressure in the liquid in the test section during depressurization from about 4 to 1 atm.

into water flowing through a capillary; the water flow transports the bubble to a smooth opening from which it is released. In this system, the use of fast-action valves permits accurate control of the bubble size.

In order to decrease the optical distortion caused by the tube, the test section is enclosed in a water-filled Plexiglas box with flat windows (figure 1*a*). The residual distortion due to the small difference between the indices of refraction of water and Plexiglas is compensated for by the calibration procedure described below. The motion of the rising bubble is recorded with a high-speed video camera (Kodak Imager CR2000) at framing rates up to 1000 frames per second. The camera is operated in the full framing mode which gives 512×384 pixels. The bubble is viewed by diffuse back-lighting illumination with a four-mirror system in order to produce views from two orthogonal directions (figure 1*b*).

Lighting is provided by two stroboscopic sources, each consisting of a packed array of 32 light-emitting diodes, and diffusers. Generally, these diodes can only withstand a current of 20–50 mA in continuous operation; however for short times (typically less than 0.1 ms), higher currents enhance the light output without damaging the semiconductor. In the present application, each diode is powered by a 0.25 A current for 23 μs at 1000 Hz. Each strobe is driven by four home-built current amplifiers providing up to 8 A for the duration of each flash. In addition to the moderate cost of this system, the diodes' high efficiency of conversion of electric energy to light has the advantage of preventing heating of the experimental set-up.

In the image processing step, the background is first subtracted from the raw images to give results like those shown in figure 3. The *CONTOURC* subroutine of *MATLAB*

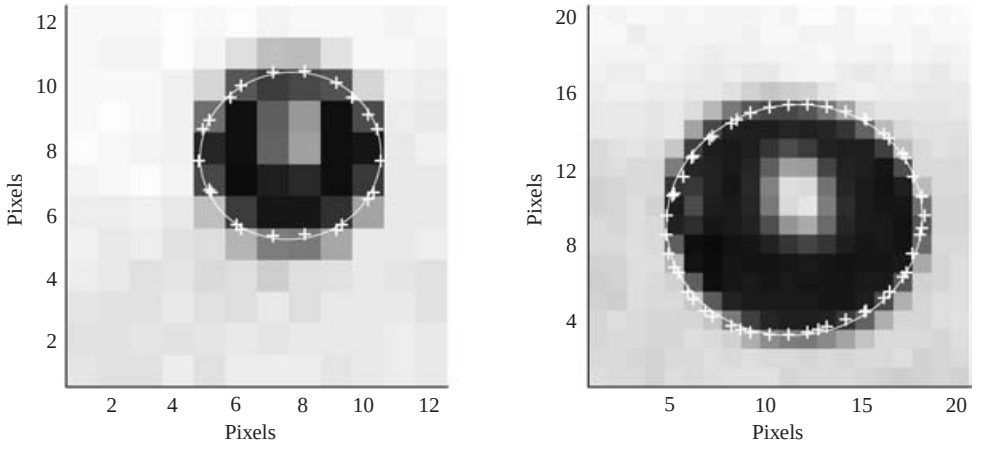

FIGURE 3. Fitting ellipsoids to the images given by the camera; the pixel size is 130 μm. The accuracy of these measurements is discussed in § 2.

is used to identify the grey-level isoline corresponding to 90% brightness marked by white crosses in the figure. This isoline is least-squares fitted with an ellipsoid, also shown in the figure, from which the equivalent spherical radius and the bubble centre are determined. Clearly, the procedure cannot determine the radius to better than half the pixel size, approximately 65 μm which, for the smallest bubbles considered here, can be up to 15% of the radius. However, as will be shown below in connection with figure 5, the actual error is smaller. The relative error (i.e. the frame-to-frame variation of the radius) is much smaller due to the homogeneity of the illumination and the low noise level of the data acquisition system. Tests conducted with a 1.15 mm-radius metal sphere falling with a speed of $0.83\,\mathrm{m\,s^{-1}}$ gave a relative error of 0.5% for the radius and 0.8% for the velocity.

The two upper lines in figure 4 show sample data of the bubble radius vs. time reconstructed in this way from each of the two views provided by the optical system for a pressure change of 3 bars. Here the thicker (upper) line is from the right view and the thinner line from the left view. The brightness and sharpness of the two views differed somewhat: the values of R reported in the following are obtained from the left view, which seemed slightly more in focus. The calibration with the solid sphere confirmed that the absolute error affecting this view was only about 15 μm.

To extract three-dimensional information from the two approximately orthogonal views the optical system needs to be calibrated. For this purpose, we view through this system, without altering the camera settings, a planar grid of black circles inserted vertically along the axis of the tube. The images of the circles are fitted to ellipsoids as before, which enables us to determine the position of their centres in the image with sub-pixel accuracy. Since the coordinates of the centres of the circles on the physical grid are known, this procedure determines the mapping of the physical coordinates of the planar grid onto the pixel coordinates in the image planes. This mapping is used to obtain the parameters of a nine-parameter pin-hole camera model using the method of Lenz & Tsai (1988). The camera models (one for each view) obtained in this way account for linear image distortion, perspective projection, and second-order radial lens distortion.

For each pixel on each of the views, the camera model determines the ray along which the corresponding point of the physical object – the object point – is situated.

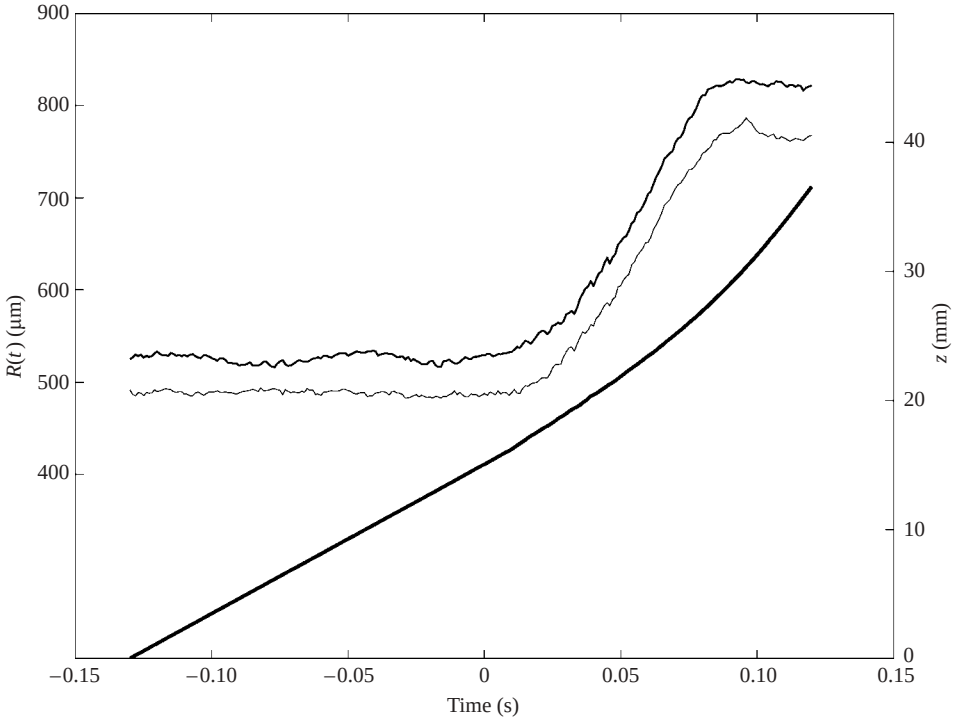

FIGURE 4. The two upper lines (the left vertical scale) are the equivalent radii as measured from the right (upper line) and left (lower line) views for $\Delta P \simeq 3$ bars (the case of figure 2). The thick solid line (the right scale) is an example of the measured vertical position vs. time for a bubble with an initial radius of 525 μm expanded with the ΔP of figure 2.

The position of the object point relative to each view is assumed to correspond to the position where the two rays are the closest (see Sonka, Hlavac & Boyle 1998 for further details). In the present situation, the bubble position in three-dimensional space is required both to measure its velocity and to determine the trajectory of its ascent (see § 5 below). A typical example of the vertical position vs. time of the bubble centre obtained from our system is shown by the thick solid line in figure 4. The rise velocity of the bubble is obtained from the slope of straight lines least-squares fitted through three consecutive data points.

The experiment is entirely computer-controlled. A counter board (PCL-830) is responsible for the triggering of the camera, the depressurization valve, and the data acquisition. The pressure sensor, the camera trigger, and the exposure time of each image are recorded with a data acquisition card (PCI-MIO16, National Instruments Inc.).

3. Force balance model

A simple model to interpret the data can be set up in terms of a force balance. The forces acting on the bubble are buoyancy, drag, and pressure gradient. For bubbles rising rectilinearly, these forces are all parallel to the (upward oriented) z-axis and, since the bubble itself has negligible mass, their sum must balance the rate of change

Figure	k	α
6	107.8	0.97
8	76.28	0.939

TABLE 1. Parameters used in (3) to calculate the steady drag force on the bubbles shown in figures 6 and 8.

of the Kelvin impulse (1); we may therefore write

$$\tfrac{2}{3}\pi\rho\,\frac{\mathrm{d}}{\mathrm{d}t}\left[R^3\,(U_B-U_L)\right] \;=\; \tfrac{4}{3}\pi R^3\rho g-\tfrac{1}{2}\pi R^2\rho C_D\,|U_B-U_L|\,(U_B-U_L)+\tfrac{4}{3}\pi R^3\rho\frac{\mathrm{d}U_L}{\mathrm{d}t}\,. \tag{2}$$

Here U_B is the velocity of the bubble and g the acceleration gravity. As explained in Appendix A, the elastic waves propagating along the tube, although of low amplitude (about 300 μm), induce a large acceleration in the liquid (about $1.5\,\mathrm{m\,s^{-2}}$).† The liquid velocity U_L is included here to account for this phenomenon and is estimated in (A 8) of Appendix A. The drag coefficient C_D is taken as

$$C_D \;=\; k\,Re^{-\alpha}, \tag{3}$$

where $Re = 2R|U_B-U_L|/\nu$ (in which ν is the liquid kinematic viscosity) is the instantaneous Reynolds number. This functional form is known to approximate the measured drag coefficient over limited ranges of bubble sizes when the radius is constant (see e.g. Maxworthy *et al.* 1996) and, in particular, with $k=48$ and $\alpha=1$, it gives the well-known large-Reynolds-number limit. The constants k and α are found by fitting the measured bubble rise velocities before and after the expansion; numerical values for the examples discussed in this paper are shown in table 1; the exponent α is close to 1, but the multiplicative constant is much larger than 48 due to water contamination (see § 5). No data exist for the viscous drag on bubbles with a variable radius. Magnaudet & Legendre (1998) have presented an analysis of the problem validated by numerical calculations. Although they do not address specifically the case of expanding bubbles, their results suggest that, at high translational Reynolds number, the use of the quasi-steady drag relation (and, in particular, the omission of the history force) is justifiable.‡ Legendre, Borée & Magnaudet (1998) also demonstrated numerically that the added mass coefficient of a growing or collapsing spherical bubble translating at finite Reynolds number is 1/2.

The instantaneous bubble radius $R(t)$ is calculated from the well-known Rayleigh–Plesset equation of bubble dynamics:

$$R\ddot{R}+\tfrac{3}{2}\dot{R}^2 \;=\; \frac{1}{\rho}\left[p-P(t)-\frac{2\sigma}{R}-4\mu\frac{\dot{R}}{R}\right], \tag{4}$$

in which dots denote time derivatives, P is the liquid pressure measured in the neighbourhood of the bubble, and μ and σ denote the liquid viscosity and interfacial

† We are indebted to Professor John Blake of the University of Birmingham for pointing out this possibility to us.

‡ More precisely, Magnaudet & Legendre find that, at high Reynolds number, the drag coefficient for spherical bubbles is given by $48/Re(t)$, in which $Re(t)$ is the Reynolds number based on the instantaneous bubble radius (the translational velocity was supposed to be constant in their analysis). The bubbles studied here are mostly spherical and the smallest Reynolds numbers are about 80.

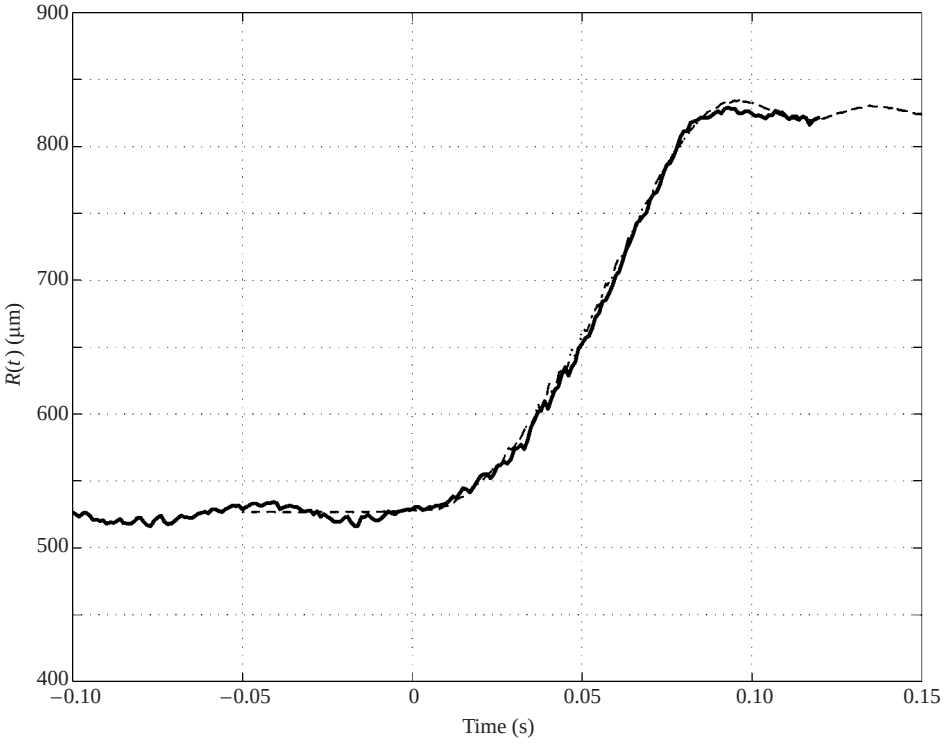

FIGURE 5. Comparison of the measured (solid line) and calculated bubble radii for the case of figure 2 with $\Delta P \simeq 3$ atm.

tension coefficient. Over the typical depressurization time of 50 ms, the thermal diffusion length in air is of the order of 1 mm, which implies that the bubble internal pressure p can be calculated assuming an isothermal expansion of the gas. The depressurization time is also much longer than the bubble volume oscillation period so that the radius could also be calculated from the quasi-equilibrium relation $R(t) = R_0 (P_0/P(t))^{1/3}$ where R_0 is the bubble radius when the pressure in the tube has the initial value P_0. Indeed, the two procedures give essentially identical results.

Figure 5 compares the time dependence of the radius given by (4) with the experimentally measured radius for the case of figure 2 with $\Delta P \simeq 3$ bars. Here again we can verify that the error in the radius measurements was actually smaller than the theoretical maximum of 15% mentioned in § 2. Indeed, one half-pixel error on the maximum radius would correspond, before expansion, to an error of about 40 μm, i.e. about 8%.

Equation (2) can be put into a more convenient form as follows:

$$\frac{\mathrm{d}U_B}{\mathrm{d}t} = 3\frac{\mathrm{d}U_L}{\mathrm{d}t} - \frac{3}{R}\frac{\mathrm{d}R}{\mathrm{d}t}(U_B - U_L) + 2g - \frac{3}{4}\frac{C_D}{R}|U_B - U_L|(U_B - U_L). \qquad (5)$$

The first term on the right-hand side includes the conventional added mass effect due to the relative acceleration (with a coefficient 1) and the pressure gradient in the liquid (with a coefficient 2). This term accounts for the well-known fact that the acceleration of a spherical bubble is three times that of the liquid (see e.g. Landau &

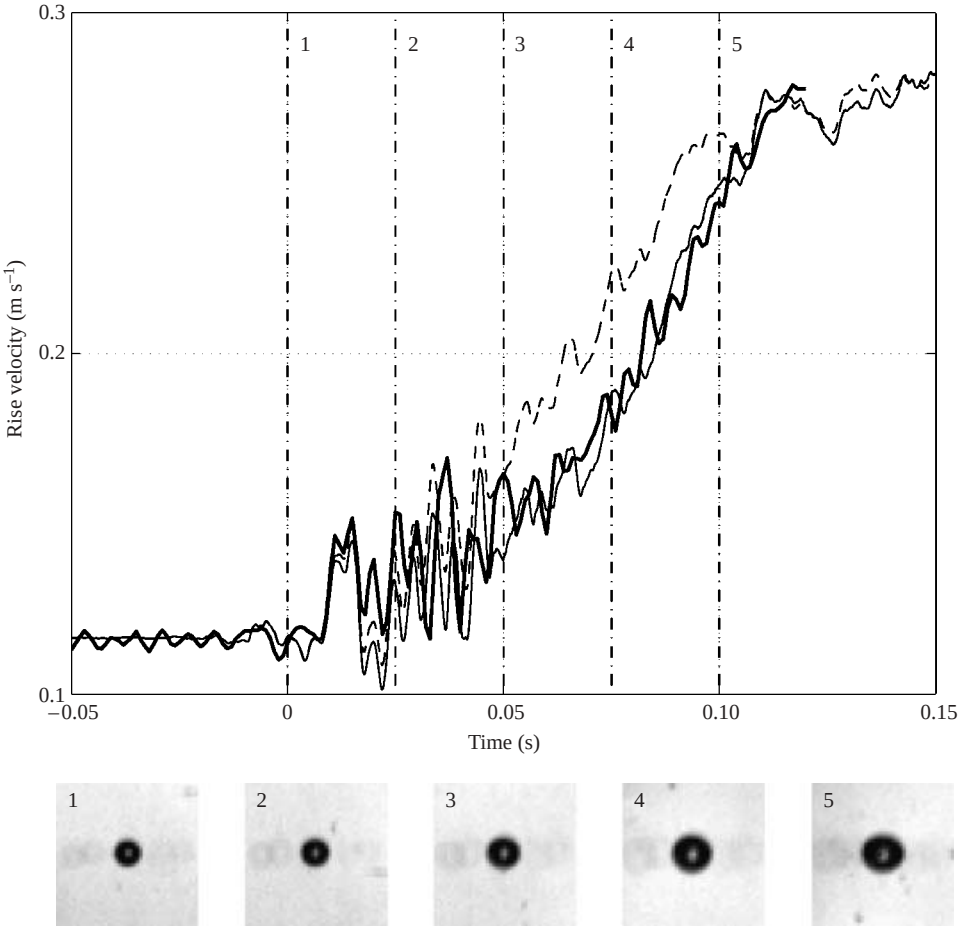

FIGURE 6. Measured bubble velocity vs. time (thick line) for the case of figure 2 with $\Delta P \simeq 3$ atm; the thin solid line is the theoretical result from (5) and the dashed line the theoretical result from (6) which does not include the effect of $\mathrm{d}R/\mathrm{d}t$ in the added mass interaction. The vertical lines mark the instants at which the photos shown at the bottom of the figure were taken.

Lifshitz 1987). The focus of the present work is the second term, which is the volume change contribution to the added mass interaction; in order to show its importance, we will compare the solutions of (5) with those of the same equation in which this term is omitted:

$$\frac{\mathrm{d}U_B}{\mathrm{d}t} = 3\frac{\mathrm{d}U_L}{\mathrm{d}t} + 2g - \frac{3}{4}\frac{C_D}{R}|U_B - U_L|(U_B - U_L). \tag{6}$$

In using the estimate (A 8) for U_L to interpret the data, we take the measured values of G, but we fit the prefactor $(z^2/D_0 z_W)$ so as to achieve the best (in the least-squares sense) agreement with the data. This procedure is justified by the several approximations that go into the derivation of (A 8). Its legitimacy is strengthened by the fact that the results of the fit are not very different from the *a priori* estimates of the prefactor that are available.

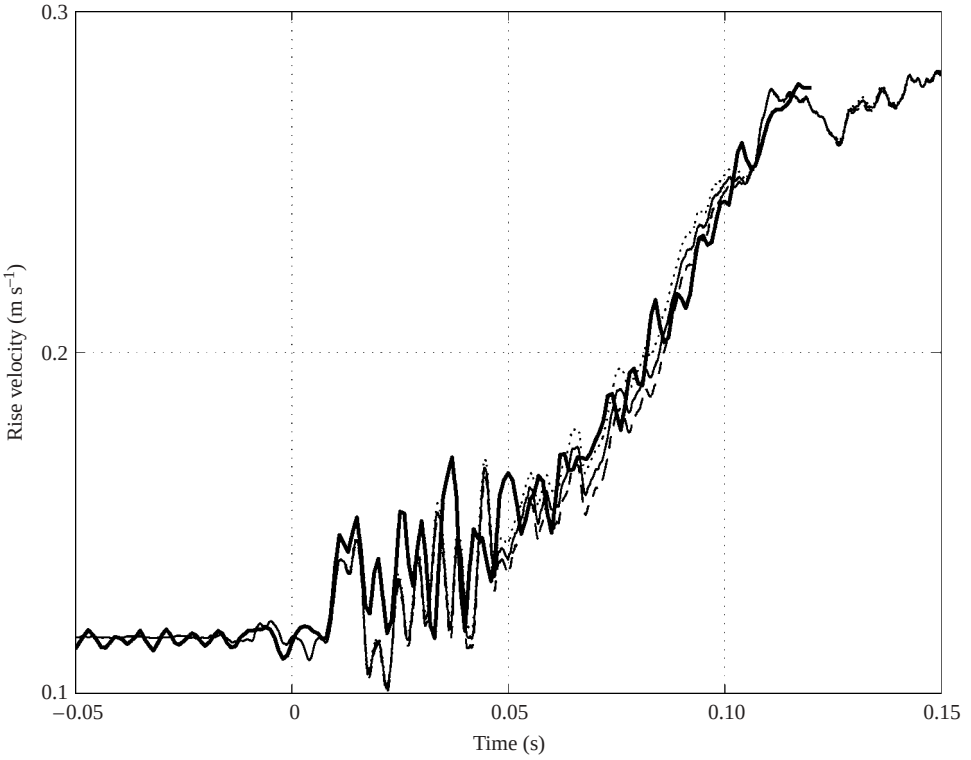

FIGURE 7. As figure 6 but the dashed line is obtained from (5) with a value of 0.6, rather than 0.5, for the added mass coefficient multiplying the $\mathrm{d}R/\mathrm{d}t$ term. The dotted line is the result of a similar calculation with 0.4 in place of 0.5.

4. Experimental results

Data were taken when the bubbles had risen about 0.15 m from the bottom of the tube. The time scale for the damping of surface modes for a 500 μm-radius bubble in water is of the order of 0.01 s and therefore, by the time data were taken, any surface oscillation due to the bubble generation had been completely damped out. As mentioned in § 2, the rise velocity of the bubble was obtained from the slope of straight lines least-squares fitted through three consecutive data points. A typical result is shown by the thick solid line in figure 6 for the same case as in figures 2, 4 and 5; the initial and final bubble radii are 525 and 825 μm. The photos under the graph are snapshots of the bubble at the times marked by vertical lines on the figure.

The high-frequency oscillations in the early part of the trace, for $t < 0$, are too slow for the natural frequency of oscillation of the bubble; they are background noise in the experiment, possibly due to the spatial discretization associated to the individual pixels of the camera. After the pressure-release valve starts to open at $t = 0$ ms, some strong oscillations are observed just before the mean rise velocity begins to change appreciably. As the bubble expands and buoyancy becomes stronger, the bubble accelerates while the oscillations, even though weaker, continue. As revealed by the photos, the bubble remains essentially spherical until the middle of the expansion, but then it acquires a clear oblate shape.

The thin line in this figure is the result of the integration of (5) in which the expression (A 10) is used for U_L with the measured tube wall displacement shown

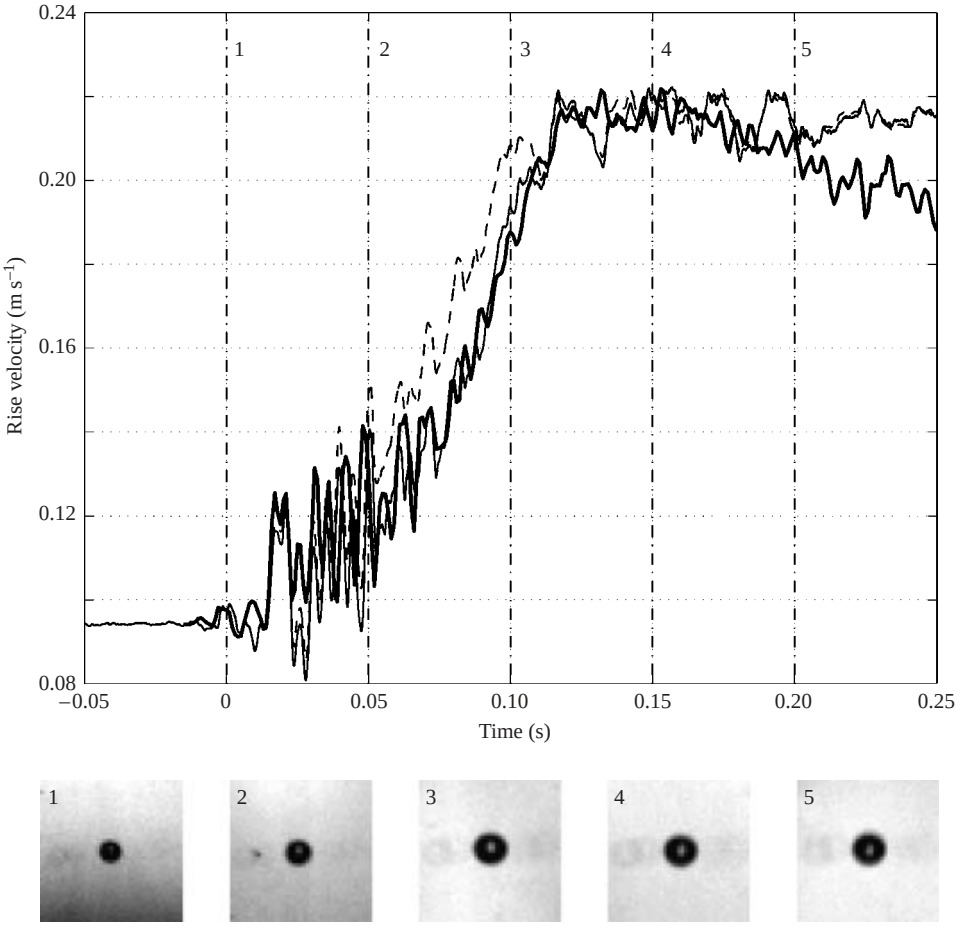

FIGURE 8. The same as figure 6 but for a different case. Note the gradual decline of the rise velocity after the expansion due to progressively increasing surface contamination.

in figure 12. (Although tube wall displacement and bubble rise were not measured simultaneously, we have verified that the tube wall motion was reproducible.) The fitted value of the parameter $(z^2/D_0 z_W)$ in (A 10) is 0.8, which is not very different from 0.63, which is what one would expect with $z = 0.15$ m, $D_0 = 60$ mm, $z_W = 0.6$ m.

The model does not capture all the details of the oscillations in the data (and, in particular, the phase seems to drift, possibly due to errors affecting the shorter waves, as discussed in Appendix A), but overall the agreement is good. If, for this case, the bubble velocity is calculated from (6), which does not include the term $\mathrm{d}R/\mathrm{d}t$, the result shown by the dashed line in figure 6 is found. It is evident that omission of this term gives results in marked disagreement with the data.

The same measured and computed velocities are shown again by the thick and thin solid lines in figure 7; here the dashed line is what the model (5) predicts if the $\mathrm{d}R/\mathrm{d}t$ term were multiplied by 0.6, in place of 0.5 (with the coefficient of $\mathrm{d}U/\mathrm{d}t$ still kept at 0.5). The two theoretical lines are fairly close and it would be hard to choose between the two values solely on the basis of these results. As expected, of course, the theoretical lines coincide at the beginning and at the end of the process, where

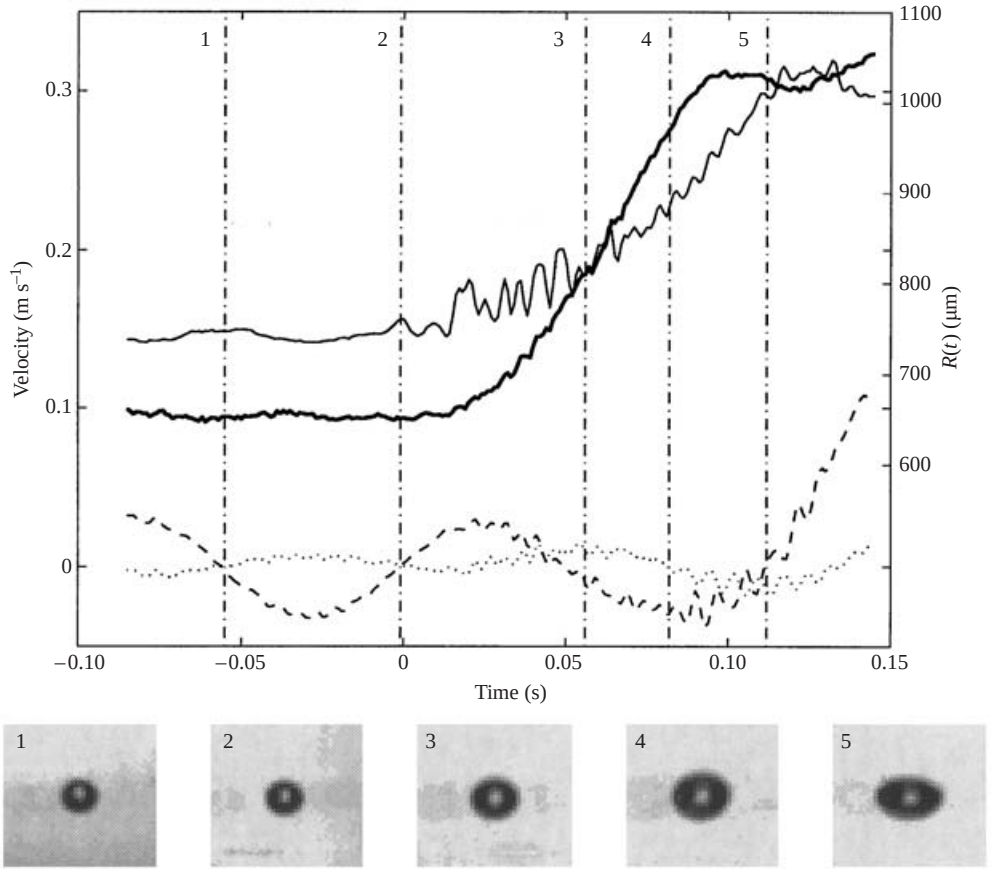

FIGURE 9. The thick line is the radius and the thin lines the three velocity components of a bubble with $\Delta P \simeq 3$ atm and initial radius of 690 μm; solid line, vertical velocity; dashed lines x-velocity; dash-and-dot line, y-velocity. The vertical lines mark time instants keyed to the photos and to figure 10.

the radial velocity is small. The dotted line is a similar calculation with a value 0.4. Analogous calculations with 0.3 and 0.7 (not shown), on the other hand, exhibit a clear difference with the data. We can test in the same way the effect of an error in the initial value of the radius before expansion: if it is changed by $\pm 15\%$, the effect on the theoretical curve is much less than that shown in figure 7 for the change in the added mass coefficient from 0.5 to 0.5 ± 0.1.

Another example similar to figure 6 is shown in figure 8, for which again $\Delta P \simeq 3$ atm; here the initial radius is 425 μm, and the final radius 670 μm. A notable feature, to which we will return in the next section, is the gradual decline of the rise velocity after the expansion.

5. Additional observations

Some further observations made in the course of this experiment are also of interest.

In water, bubbles with a radius greater than about 0.6–0.7 mm rise along a zig-zag or spiralling path (see e.g. Saffman 1956; Clift, Grace & Weber 1978; Lunde

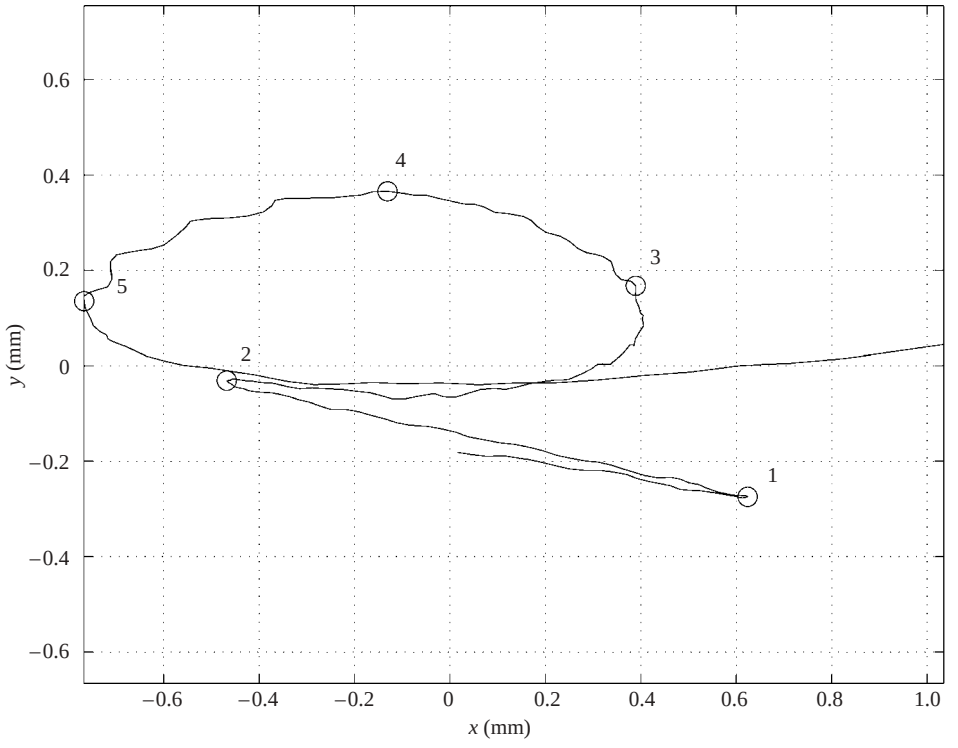

FIGURE 10. Projection on the horizontal plane of the trajectory of the bubble of figure 9: note the rapid transition from a zig-zag to a helical path. The numbers refer to the time instants marked by the vertical lines in figure 9.

& Perkins 1998; Brücker 1999; de Vries 2001; Ellingsen & Risso 2001; Mougin & Magnaudet 2002; de Vries, Biesheuvel & van Wijngaarden; and references therein), an effect which may be referred to as *Leonardo's paradox* (see Appendix B). Since in our experiment the bubble diameter increases by rather large factors, we can easily observe the transition from straight to non-rectilinear ascent, and the effect of bubble expansion on a non-rectilinear ascent.

An example is shown in figures 9 and 10 (initial radius 690 μm, final radius 1080 μm, with $\Delta P \simeq 2.8$ bars). The three components of velocity and the radius (thick solid line) are shown as functions of time in figure 9, while figure 10 is a projection of the bubble trajectory on a horizontal plane. The bubble is large enough to have a zig-zag motion in its compressed state, but it very rapidly (less than 50 ms) transitions to a spiral motion before the expansion is completed.

Another interesting effect has already been noted in connection with figure 8, in which the bubble rise velocity is seen to reach a maximum at the end of the expansion, and then to gradually decrease stabilizing at a lower value. To a varying degree, this phenomenon was quite common and was found to be sensitive to the time the water had been standing in the tube. This circumstance points to an effect of contamination, chiefly by the soluble plasticizers leaching out of the Plexiglas. When the bubble expands, fresh air–liquid interface is generated; as the bubble rises, however, impurities collect again on the bubble surface, the drag increases, and the velocity decreases.

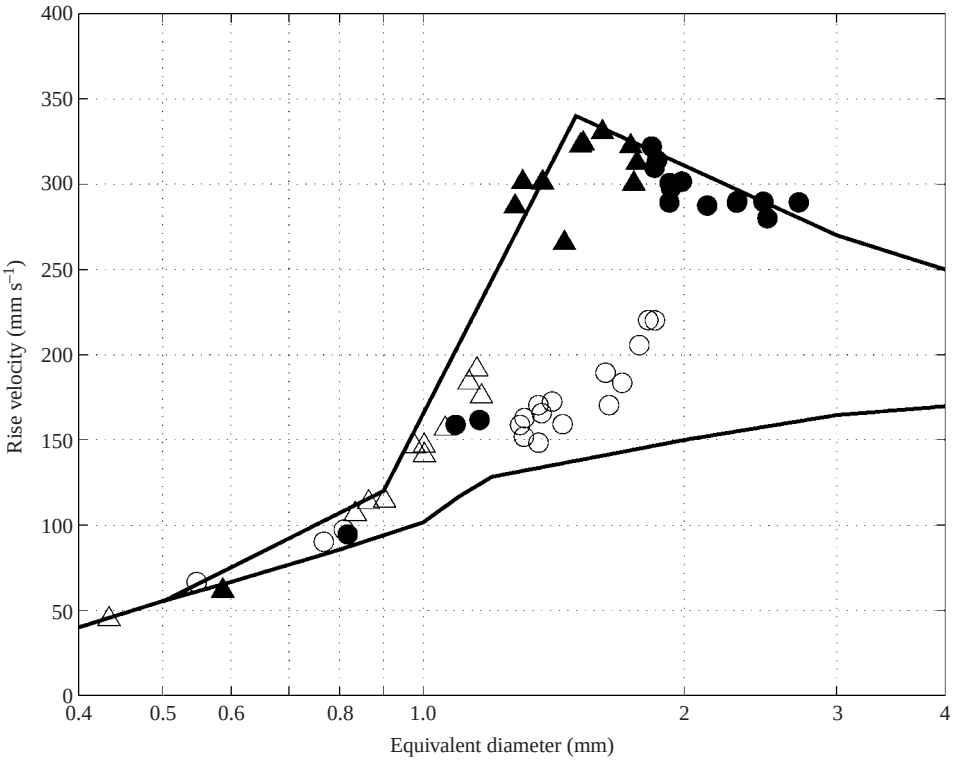

FIGURE 11. The upper curve (from Clift *et al.* 1978) is the rise velocity of bubbles in clean water, the lower curve in heavily contaminated water. The open and closed symbols are velocities measured before and after the expansion, respectively. Triangles are data for experiments conducted in a freshly filled tube, while circles indicate rise velocity data taken in water that had been standing in the tube for days. Even for these contaminated bubbles, after the expansion the freshly formed surface is clean and the rise velocity is close to the value expected for a clean bubble.

To further illustrate the point, we collect in figure 11 several observations of the bubble rise velocity before (open symbols) and immediately after the expansion: here the lines are approximations to the results of Gaudin (as reproduced in figure 99 of Clift *et al.* 1978) and mark the range of observed rise velocities of air bubbles in clean (upper line) and contaminated (lower line) water. Triangles are data for experiments conducted in a freshly filled tube, while circles indicate rise velocity data taken in water that had been standing in the tube for days. Before expansion (open symbols), the former group of data is clearly closer to the clean-bubble line than the latter group. Immediately after expansion, on the other hand, the distinction between the two groups of data disappears and both cluster close to the clean bubble line.

6. Conclusions

We have described the results of an experiment to study the volume-change term in the added mass interaction of a bubble rising in a liquid. The results clearly confirm the importance of this term and are compatible with the usually accepted value for its coefficient, even though the accuracy of the experiment is not sufficient to pinpoint this value to better than about 20%.

The results also afford a new way to study the instability responsible for *Leonardo's paradox*, namely the instability of the rectilinear trajectory of a rising bubble. While we have not pursued this aspect of the phenomenon in this paper, we have observed that the growth rate of the instability after the expansion of the bubble is very rapid, as can be seen for example in figure 10. The results also clearly demonstrate the effect of surface contamination and the drag reduction that accompanies the formation of a fresh interface immediately after the bubble expansion.

It would of course also be of interest to study the opposite case of a contracting bubble. This problem would however be more complicated both experimentally, since the already small bubbles necessary to operate in the rectlinear ascent regime would become even smaller, and theoretically, due to the possible development of jets traversing the bubble.

The authors express their gratitude to Professor John Blake, Professor Leen van Wijngaarden, and Professor Detlef Lohse for suggestions and discussions. This study has been supported by the Fundamenteel Onderzoek der Materie of The Netherlands under grant No. 99MFS06.

Appendix A. Tube expansion

When the high pressure is released, elastic waves propagate along the tube until, by the time they have dissipated, the tube diameter is slightly smaller than it was when pressurized. Even though the amplitude of these waves is less than 300 μm, their frequency is large enough to cause a significant acceleration of the liquid with a correspondingly large effect on the bubble behaviour. This effect can be approximately accounted for as follows.

We assume that elastic waves propagating along the tube are linear and axisymmetric and write

$$D(z,t) = D_0 + F\left(t - \frac{z}{c}\right) - F\left(t + \frac{z}{c}\right), \tag{A 1}$$

where D is the local instantaneous tube diameter and c is the wave speed. In writing this relation we have assumed that the tube is clamped at the bottom $z = 0$ so that its diameter there maintains the undisturbed value D_0. Although it will not be necessary to know the wave speed c, it is useful to have an estimate for this quantity, which we obtain by using the result (see e.g. Lighthill 1978, pp. 93, 96)

$$c^2 \simeq \frac{hE}{D_i \rho}, \tag{A 2}$$

where D_i is the tube internal diameter, h the wall thickness, and E the Young modulus of the tube material; for the present experiment $D_i = 50\,\mathrm{mm}$, $h = 5\,\mathrm{mm}$, and $E = 3.3\,\mathrm{GPa}$, so that $c \simeq 574\,\mathrm{m\,s^{-1}}$.

Consider a fluid particle which, in undisturbed conditions, is located at a height z above the bottom of the tube. When waves travel along the tube, by conservation of mass this fluid particle will be at a height $Z(z,t)$ from the tube bottom such that

$$\frac{\pi}{4}\int_0^Z D^2(\zeta,t)\,\mathrm{d}\zeta = \frac{\pi}{4}\int_0^z D_0^2\,\mathrm{d}\zeta\,. \tag{A 3}$$

Upon taking the time derivative of this relation we find

$$\frac{\partial Z}{\partial t} = -\frac{2}{D^2(Z,t)} \int_0^Z D \frac{\partial D}{\partial t} \, \mathrm{d}\zeta \,, \tag{A 4}$$

or, since the tube deformation is small,

$$\frac{\partial Z}{\partial t} \simeq -\frac{2}{D_0} \int_0^z \frac{\partial D}{\partial t} \, \mathrm{d}\zeta \,. \tag{A 5}$$

But, from (A 1),

$$\frac{\partial D}{\partial t} = -c \frac{\partial}{\partial z} \left[F\left(t - \frac{z}{c}\right) + F\left(t + \frac{z}{c}\right) \right], \tag{A 6}$$

which enables us to evaluate the integral in (A 5) with the result

$$\frac{\partial Z}{\partial t} = \frac{2c}{D_0} \left[F\left(t - \frac{Z}{c}\right) + F\left(t + \frac{Z}{c}\right) - 2F(t) \right] . \tag{A 7}$$

A further approximation can be made by noting that the spatial spectrum of the waves will contain harmonics of the order of L/n, where $n = 1, 2, \ldots$, and L is the length of the tube. During the present measurements, the bubble is near the bottom of the tube ($z \simeq 0.1$ m) and, therefore, $Z \ll L$. Thus, we may assume that Z will be smaller than the wavelength of at least the lowest harmonics. This circumstance justifies an expansion of the first two terms in (A 7) in a Taylor series. Furthermore, since the particle displacement is small, we may set $Z \simeq z$ in the result to find

$$\frac{\partial Z}{\partial t} \simeq \frac{2}{D_0 c} F''(t) \, z^2. \tag{A 8}$$

This procedure will not be accurate for the higher Fourier modes, which accounts for the differences at the higher frequencies mentioned before. The previous analysis shows, however, that the resulting error remains manageable.

During the depressurization, the tube wall displacement is measured at a single position z_W with a laser beam reflected from the tube surface at an angle of 42° in a vertical plane. The position of the reflected beam is recorded with the high-speed camera, and transferred to a computer. The CCD chip of the camera serves as a position-sensitive device and, therefore, no imaging lens is used. After post-processing the images and extracting the position of the centre of the laser spot, the function $D(z_W, t)$ is obtained from simple geometrical optics considerations knowing that the size of the individual pixels of the chip is 20 μm. Effecting in (A 1) the same expansion that lead to (A 8), we may say that what is actually measured is

$$G(t) \simeq D_0 - 2\frac{z_W}{c} F'(t), \tag{A 9}$$

so that we may rewrite (A 8) as

$$\frac{\partial Z}{\partial t} \simeq -\frac{z^2}{D_0 z_W} G'(t). \tag{A 10}$$

An example of the measured $G(t) - D_0$ (panel *a*, solid line), $G'(t)$ (*a*, dashed line) and $G''(t)$ (panel *b*) for the pressure change of $\Delta P \simeq 3$ bar of figure 2 is shown in figure 12. The major feature in this figure is the monotonic expansion of the tube, but the presence of higher-frequency oscillations due to the waves propagating along the tube is also clearly visible. The amplitude of the velocity oscillations is about

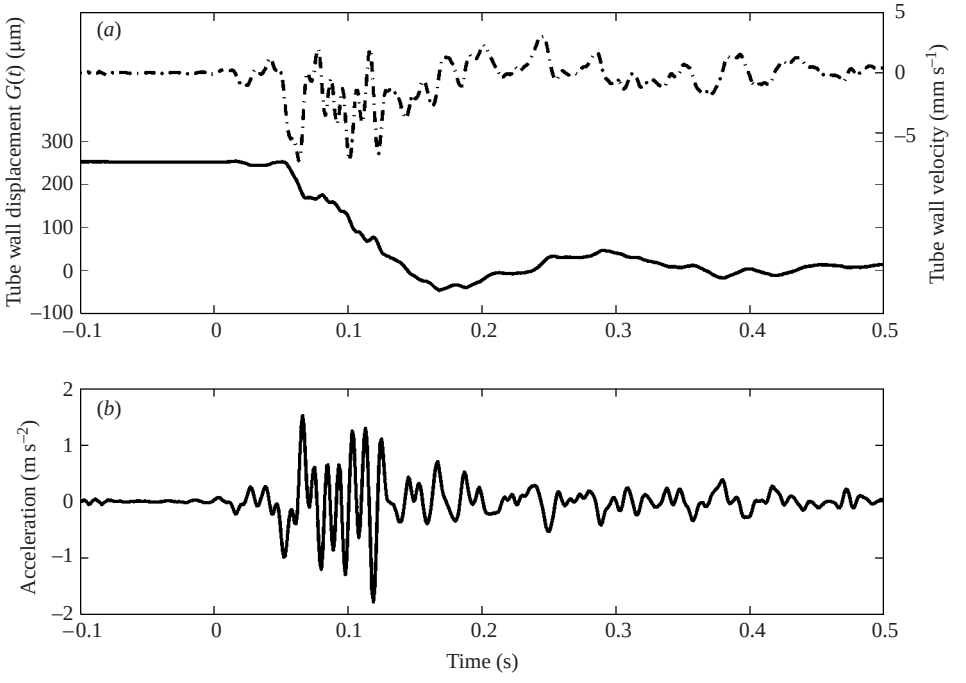

FIGURE 12. (*a*) Measured displacement of the tube wall during depressurization (solid line) and corresponding radial velocity for the depressurization of figure 2; (*b*) the radial acceleration of the tube wall.

$5\,\mathrm{mm\,s^{-1}}$ but, due to the presence of high frequencies, the maximum acceleration is of the order of $1.5\,\mathrm{m\,s^{-2}}$.

Appendix B. Leonardo's paradox

By A. Prosperetti[1], *C. D. Ohl*[1], *A. Tijink*[1], *G. Mougin*[2] *and J. Magnaudet*[2]
[1]*Department of Applied Physics, Twente Institute of Mechanics and Burgerscentrum, University of Twente, AE 7500 Enschede, The Netherlands*
[2]*Institut de Mécanique des Fluides de Toulouse, UMR CNRS/INPT/UPS 5502, 2 Allée Camille Soula, 31400 Toulouse France*

Several annotations in Leonardo da Vinci's notebooks are possibly the first scientific reference to the fact that, in water, bubbles with a diameter of a few millimetres do not rise along rectilinear paths. For example, on fol. 25 *r* of the *Codex Leicester* (formerly Hammer; see Roberts 1981), in which the sketch reproduced in figure 13 is found, he writes (McCurdy 1938, Vol. 1, p. 112):

> The air which is submerged together with the water... returns to the air, penetrating the water in sinuous movement... And this occurs because the light thing cannot remain under the heavy... ; and because the water that stands there perpendicular is more powerful than the other in its descent, this water is always driven away by the part of the water that forms its coverings, and so moves continually sideways where it is less heavy and in consequence offers less resistance... And because this has to make its movement by the shortest way it never spreads itself out from its path except to the extent to which it avoids that water which covers it above.

FIGURE 13. Leonardo's sketch of a helically rising bubble from fol. 25 *r* of the Codex Leicester (reproduced with the kind permission of the Armand Hammer Foundation from an exhibition catalogue published in 1982).

A similar passage can be found in Manuscript F, fol. 37 *r*, accompanied by the sketch reproduced in figure 14 (from Ravaisson-Mollien 1889) (McCurdy 1938, Vol. 1, p. 557):

> Whether the air escapes from beneath the water by its nature or through its being pressed and driven by the water.
>
> The reply is that since a heavy substance cannot be supported by a light one this heavy substance will proceed to fall and seek what may support it, because every natural action seeks to be at rest; consequently that water which surrounds this air above, on the sides and below finds itself all spread against the air enclosed by it, and all that which is above *d e n m*, [the reference is to the sketch reproduced in figure 14] pushes this air downwards, and would keep it below itself if it were not that the laterals *a b e f* and *a b c d* which surround this air and rest upon its sides came to be a more preponderant weight than the water which is above it; consequently this air escapes by the angles *n m* either on one side or on the other, and goes winding as it rises.

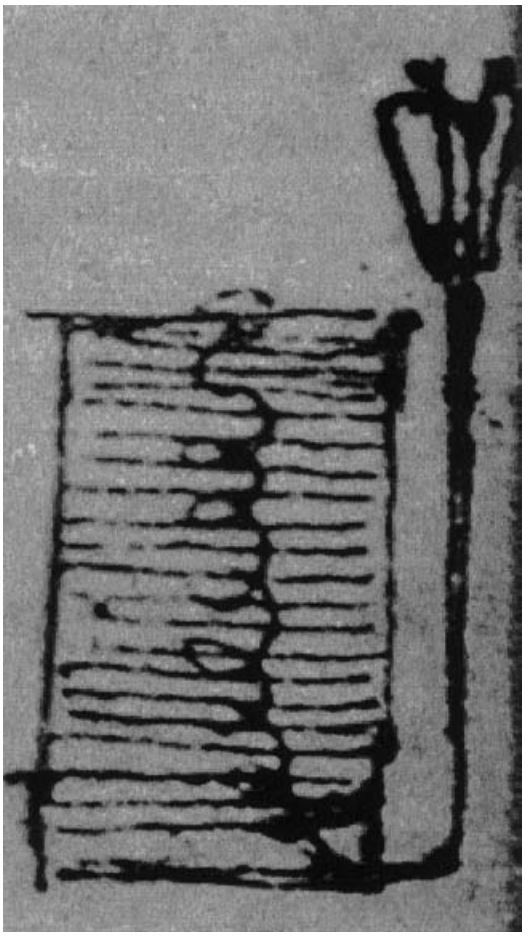

FIGURE 14. Another sketch by Leonardo of a helically rising bubble from Manuscript F, fol. 37 *r* (reproduced from Ravaisson-Mollien 1889).

Leonardo was intrigued by the phenomenon as part of his broader interest in Mechanics. He was a follower of the *impetus* theory†, according to which (I, 68 [20] r; McCurdy 1938, Vol. 1, p. 76):

> Every natural and continuous movement desires to preserve its course on the line of its inception, that is, however its locality varies, it proceeds according to its beginning.

This tendency (which differs from that of Newtonian mechanics in that it was thought that velocity, rather than acceleration, was proportional to force) required an explanation for the curved path of bubbles and similar phenomena. For example, in Manuscript F, fol. 52 *r*, he writes (McCurdy 1938, Vol. 1, pp. 558/559):

> If every movable thing pursues its movement along the line of its commencement, what is that causes the movement of the arrow or thunderbolt to swerve and bend in so many directions whilst still in the air? What has been said may spring from two

† "Impetus is a power transmitted from the mover to the movable thing", Cod. Atl. 219 v. *a* (McCurdy 1938, Vol. 1, p. 529).

causes, one of which ... is as in the third [section] of the fifth [book] concerning water, where it is shown how sometimes the air issuing out of the beds of swamps in the form of bubbles comes to the surface of the water with sinuous curving movement.

All these explanation are in keeping with his general principle that (Cod. Atl. 315 r. *b*; McCurdy 1938, Vol. 1, p. 532).

Every impetuous movement bends towards the less resistance as it flies from the greater.

A great deal of research has been devoted to Leonardo's contributions to Mechanics. The classic studies are those of Duhem (1906–1913); see also Somenzi (1954), Hart (1963), Kemp (1981), and others.

REFERENCES

Benjamin, T. B. & Ellis, A. T. 1966 The collapse of cavitation bubbles and the pressures thereby produced against solid boundaries. *Phil. Trans. R. Soc. Lond.* A **260**, 221–240.

Brücker, C. 1999 Structure and dynamics of the wake of bubbles and its relevance to bubble interaction. *Phys. Fluids* **11**, 1781–1796.

Clift, R. C., Grace, J. R. & Weber, M. E. 1978 *Bubbles, Drops, and Particles.* Academic.

Duhem, P. M. M. 1906–1913 *Études sur Léonard de Vinci*, vols. 1–3. Hermann, Paris.

Ellingsen, K. & Risso, F. 2001 On the rise of an ellipsoidol bubble in water: oscillatory paths and liquid-induced velocity. *J. Fluid Mech.* **440**, 235–268.

Hart, J. B. 1963 *The Mechanical Investigations of Leonardo da Vinci.* University of California Press, Berkeley CA.

Kemp, M. 1981 *Leonardo da Vinci, The Marvelous Works of Nature and Man.* Harvard University Press.

Lamb, H. 1932 *Hydrodynamics*, 6th edn. Cambridge University Press.

Landau, L. D. & Lifshitz, E. M. 1987 *Fluid Mechanics*, 2nd edn. Butterworth-Heinemann.

Legendre, D., Borée, J. & Magnaudet, J. 1998 Thermal and dynamic evolution of a spherical bubble moving steadily in a superheated or subcooled liquid. *Phys. Fluids* **10**, 1256–1272.

Lenz, R. K. & Tsai, R. Y. 1988 Techniques for calibration of the scale factor and image center for high-accuracy 3-D machine vision metrology. *IEEE Trans. Pattern Anal. Machine Intell.* **10**, 713–720.

Lhuillier, D. 1982 Forces d'inertie sur une bulle en expansion se déplaçant dans un fluid. *C. R. Acad. Sci. Paris* II **295**, 95–98.

Lighthill, J. 1978 *Waves in Fluids.* Cambridge University Press.

Lunde, K. & Perkins, R. J. 1998 Shape oscillations of rising bubbles. *Appl. Sci. Res.* **58**, 387–408.

Magnaudet, J. & Eames, I. 2000 The motion of high-Reynolds-number bubbles in inhomogeneous flows. *Annu. Rev. Fluid Mech.* **32**, 659–708.

Magnaudet, J. & Legendre, D. 1998 The viscous drag on a spherical bubble with a time-dependent radius. *Phys. Fluids* **10**, 550–554.

Maxworthy, T., Gnann, C., Kürten, M. & Durst, F. 1996 Experiments on the rise of air bubbles in clean viscous liquids. *J. Fluid Mech.* **321**, 421–441.

McCurdy, E. 1939 *The Notebooks of Leonardo da Vinci*, vols. 1 and 2. Reynal & Hitchcok, New York.

Mougin, G. & Magnaudet, J. 2002 Path instability of a rising bubble. *Phys. Rev. Lett.* **88**, 014502 (document number).

Ohl, C. D. 2001 Generator for single bubbles of controllable size. *Rev. Sci. Instrum.* **72**, 252–254.

Ravaisson-Mollien, C. 1889 *Les Manuscrits de Léonard de Vinci avec Transcription Littérale, Traduction Française et Table Méthodique*, Volume IV, *Manuscrit F de l' Institut*. Bibliotheque de l'Institut du Louvre.

Roberts, J. 1981 *The Codex Hammer of Leonardo da Vinci.* Giunti Barbera, Florence, Italy.

Saffman, P. G. 1956 On the rise of small air bubbles in water. *J. Fluid Mech.* **1**, 249–275.

Sherwood, J. D. 1999 The force on a growing bubble in potential flow. *Intl J. Multiphase Flow* **25**, 705–713.

Somenzi, V. 1954 Leonardo ed i principî della dinamica. In *Leonardo, Saggi e Ricerche* (ed. A. Marazza *et al.*). Istituto Poligrafico dello Stato, Rome, Italy.

Sonka, M., Hlavac, V. & Boyle, R. 1998 *Image Processing, Analysis, and Machine Vision*, 2nd edn. PWS Publishing, Pacific Grove CA.

de Vries, A. W. G. 2001 Path and wake of a rising bubble. PhD thesis, University of Twente, Enschede, The Netherlands.

de Vries, A. W. G., Biesheuvel, A. & van Wijngaarden, L. 2002 Notes on the path and wake of a gas bubble rising in pure water. *Intl J. Multiphase Flow* **28**, 1823–1835.

Wallis, G. B. 1989 Inertial coupling in two-phase flow: macroscopic properties of suspensions in an inviscid fluid. *Multiphase Sci. Technol.* **5**, 239–361.

Yang, B., Prosperetti, A. & Takagi, S. 2003 Numerical simulation of a rising and expanding bubble. *Phys. Fluids*, in press.